© by PSP Volume 30– No. 09/2021 pages 10482-10491 Fresenius Environmental Bulletin

FABRICATION OF SEMICONDUCTOR PHOTOCATALYST AND ITS HIGH PHOTOCATALYTIC PERFORMANCE UNDER VISIBLE LIGHT IRRADIATION

Guangyu Wu, Fang Ma, Ruofan Xiong, Zhouzhou Xu, Pingping Li, Jiangang Han, Weinan Xing*

College of Biology and the Environment, Co-Innovation Center for the Sustainable Forestry in Southern China, Nanjing Forestry University, Nanjing 210037, China

ABSTRACT

Recent years, photocatalytic technology is a compassionate of eco-friendly methods that has displayed significant consideration in the environmental fields. In this work, a series of high-performance Ag_2WO_4/WO_3/RGO photocatalysts (AWR) were synthesized through a facile hydrothermal approach. The products were characterized by using X-ray diffraction (XRD), scanning electron microscopy (SEM), Raman spectra, UV-vis diffuse reflectance spectroscopy (DRS), photoluminescence (PL) spectra, X-ray photoelectron spectroscopy (XPS) and Brunauer-Emmett-Teller (BET) nitrogen adsorption apparatus. The results indicated that the as-prepared Ag_2WO_4/WO_3 particles were distributed on the surface of RGO sheets and the introduction of RGO could narrow the band gap of Ag_2WO_4/WO_3. By using decontaminations of methyleneblue (MB) model reactions, the photocatalytic efficiencies of AWR photocatalysts were evaluated. The AWR photocatalysts exhibited superior photocatalytic activity under visible light irradiation. The photocatalytic activities of all AWR photocatalysts were higher than those of the WO_3, Ag_2WO_4 and Ag_2WO_4/WO_3 and about 98.15% MB was removed in 180 min. The possible mechanism of photocatalytic activity enhancement was proposed. The current work shows a design and synthesis of stable and high efficiency photocatalysts, applicable for the removal of the environmental organic pollutants.

KEYWORDS:
Photocatalyst, visible light irradiation, methyleneblue

INTRODUCTION

In the past decades, semiconductor-based photocatalysis has received growing attention as a promising and green technology for air and water purification [1]. Solar energy is believed as one of promising alternatives of fossil fuels due to its sustainability, abundance, easy accessibility, and environmentally friendly properties [2,3]. Among various methods of using solar energy, photocatalytic technology has been widely concerned in the treatment of environmental pollutants. As is well known, the photocatalysts can degrade organic pollutants into non-toxic molecules under light irradiation. The process of photodegradation involves photogenerated electrons and holes separating, migrating to the surface of photocatalyst materials, and then decomposing adsorbed organic molecules by a series of complicated redox reaction [4].

Recently, silver-based visible-light-driven photocatalytic semiconductor materials have received considerable attention owing to their excellent chemical stability, physicochemical property, and potential applications [5,6,]. However, silver-based photocatalyst has the limited quantum efficiency because of its wide band gap and the low separation rate of the photoexcited electron-hole in the using the visible light. Reduced graphene oxide (RGO) has attracted attention due to its attractive properties such as chemical and physical stability and an appropriated band edge potential to carry out redox reactions, in addition to non-toxicity and a simple and low-cost method of synthesis [7]. It has also received considerable attention recently for photoelectron-chemical and photocatalytic applications due to its extremely high specific surface area, high thermal, chemical stability, and fast electron transfer ability, which can effectively inhibit the recombination of the electron-hole pairs [8]. Thence, RGO can be as one of the most ideal supports for the separation and transfer of the photogenerated charge carriers [9]. In this work, Ag_2WO_4/WO_3/RGO photocatalyst (AWR) was synthesize by using a facile hydrothermal method. The degradation effect on the decomposition of methyleneblue (MB) under visible-light irradiation over the as-prepared photocatalyst were investigated. The present work provides a design and synthesis of stable and high efficiency photocatalysts, applicable for the removal of the environmental organic pollutants.

MATERIALS AND METHODS

Materials. Potassium permanganate ($KMnO_4$), lead acetate ($Pb(AC)_2 \cdot H_2O$), hydrogen peroxide (H_2O_2), sodium tungstate (Na_2WO_4), nitrate (HNO_3), sodium nitrate ($NaNO_3$), silver nitrate ($AgNO_3$), concentrated sulfuric acid (H_2SO_4), hydrochloric acid (HCl) and sodium bicarbonate ($NaHCO_3$) were purchased from Aladdin Chemical Reagent Co., Ltd. Methylene blue ($C_{16}H_{18}ClN_3S$, M_w=319.86 g mol^{-1}, MB) was purchased from Shanghai Chemical Reagent Co. Ltd.

Preparation of Ag_2WO_4/WO_3/RGO photocatalyst (AWR). Graphene oxide (GO) nanosheets were prepared according to the modification of Hummers' method from natural graphite [10]. GO (120 mg) was added to ultrapure water (120 mL), and then was sonicated for 3 h to obtain a GO aqueous suspension.

Na_2WO_4 (1.31 g) and $Pb(AC)_2 \cdot H_2O$ (1.51 g) were dissolved in 50 mL of ethylene glycol (EG) solution. The suspension was further stirred for 10 min and then was transferred into a Teflon-lined stainless-steel autoclave, which was heated at 160 °C for 12 h. After slow cooling to room temperature, the product was filtered and washed several times with alcohol/water mixture (V/V=1:1). The $PbWO_4$ precursor was obtained. The $PbWO_4$ precursor was firstly immersed in a certain amount of HNO_3 solution (4 mol L^{-1}) for 48 h. Then, the precipitate (H_2WO_4) was filtered, washed with distilled water, and dried in air. After then, the product was put into a quartz crucible with a cover and calcined at 500 °C for 2 h. The hollow sphere WO_3 was obtained.

A certain concentration of $AgNO_3$ solution was stirred under vigorous magnetic stirring. Subsequently, a certain amount of $NaHCO_3$ (3 mmol) was added dropwise into above aqueous. The suspension was continuously stirred for 1 h at room temperature to ensure complete reaction. The obtained products were collected by filtering and washed with distilled water and ethanol several times. Finally, sample was dried in a vacuum at 60 °C for 10 h and Ag_2CO_3 was obtained. A certain amount of GO aqueous suspension, WO_3 and Ag_2CO_3 were mixed and ground in an agate pestle for 30 min. Then, the mixture was calcined at 500 °C for 2 h and cooled to room temperature. The heterojunction structure Ag_2WO_4/WO_3/RGO photocatalyst was obtained. According to the dosage of GO in the samples, the three products with different mass content of RGO were prepared and expressed as AWR-1 (6.0%), AWR-2 (12.0%) and AWR-3 (18.0%), respectively.

The pure Ag_2WO_4 photocatalyst was prepared using mass content 1:1 of Ag_2CO_3 to WO_3. The Ag_2WO_4/WO_3 (the mass ratio of Ag_2CO_3 to WO_3=30%) product was also prepared by the same method without addition of GO.

Characterizations. X-ray diffraction (XRD) patterns of the AWR were obtained on the Shimadzu LabX-6000. X-ray Diffractometer (40 kV, 30 mA, λ= 0.154 nm) with a Cu K_α radiation source at a scanning rate of 4°/min within the range of 5-80°. Scanning electron microscopy (SEM) was performed on a field emission scanning electron microscope (HITACHI UHR FE-SEM SU8000, Hitachi, Tokyo, Japan) with the samples sputter-coated with 10 nm platinum. Raman spectra were recorded on a DXR Smart Raman spectrometer (Renishaw In Via) in the backscattering geometry with an excitation laser source (532 nm). UV-vis diffuse reflectance spectroscopy (DRS) was carried out on a Hitachi UV-3010 UV-vis spectrophotometer. $BaSO_4$ was as reference sample. The photoluminescence (PL) spectra were carried out on a Varian Cary Eclipse fluorescence spectrophotometer (Australia Varian co., LTD). The photocurrents were measured with an electrochemical analyzer (CHI660B, CHI Shanghai, Inc.). The X-ray photoelectron spectroscopy (XPS) of sample was performed on the ESCALAB250 XPS spectrometer with an Al Ka monochromatized source. The Brunauer-Emmett-Teller (BET) specific surface areas (S_{BET}) of the samples were carried out based on nitrogen adsorption and desorption isotherms (Micromeritics ASAP 2030 nitrogen adsorption apparatus, USA).

Photocatalytic degradation. The photocatalytic activity of AWR photocatalyst was evaluated by the degradation of dye (MB) aqueous solution under visible-light irradiation. 50 mg photocatalyst was added to 100 mL 1.0×10^{-5} mol·L^{-1} dye solution under magnetic stirring. The light source was a 250W metal halide lamp equipped with wavelength cut off filters for λ=420 nm. The photocatalytic activity of the prepared samples was performed at ambient temperature [11]. The suspensions were stirred in the dark for 30 min to reach adsorption-desorption equilibrium. After visible light irradiation, the powder was then separated by centrifugation, and the concentration of dye was determined by measuring the absorbance (465 nm) using an UV-2450 spectrophotometer. The removal efficiency of dye was calculated and photocatalytic process was modeled using pseudo first-order kinetics equation according to the following Equations (1) and (2):

$$D = \frac{C_o - C}{C_o} \times 100\% \quad (1)$$

$$\ln(C_0/C) = kt \quad (2)$$

where D is the removal efficiency; C_0 (mg·L^{-1}) is the initial concentration of original dye solution; C

($mg \cdot L^{-1}$) is the dye concentration after light irradiation at time t (min). k is the apparent rate constant.

The reusability is an important parameter of the photocatalytic process. In order to examine the photocatalytic stability of the photocatalyst, AWR ternary plasmonic photocatalyst was filtered and washed with distilled water several times and dried in a vacuum oven at 60 °C for 12 h. The AWR photocatalyst was repeated the above cycles for five times under the same reaction conditions.

RESULTS AND DISCUSSION

Characterization. XRD patterns of pure WO_3 (a), Ag_2WO_4 (b), Ag_2WO_4/WO_3 (c), AWR-1 (d), AWR-2 (e) and AWR-3(f) photocatalysts are shown in Figure 1. From Figure 1a, the WO_3 is in good agreement with orthorhombic phase of WO_3 indexed to be the data in the JCPDS card (No. 20-1324) [12]. The diffraction peaks of Ag_2WO_4 are identical to the orthorhombic phase of Ag_2WO_4 in the JCPDS card (No. 34-0061) [13]. The pure Ag_2WO_4 (Figure 1b) displays sharp diffraction peaks at 2θ values of 16.71, 30.27, 31.63, 33.09, 45.45, 54.65 and 58.16° correspond to the planes of (011), (002), (231), (400), (402), (361) and (333), respectively. It is noteworthy that the peak intensity (2θ=31.63°) is stronger compared to other diffraction peaks. For Ag_2WO_4/WO_3 composite (Figure 1c), the diffraction peaks of Ag_2WO_4 and WO_3 are also clearly observed in comparison with bare Ag_2WO_4 and WO_3. Almost all the diffraction peaks of AWR photocatalysts (Figure 1d-f) can be assigned to Ag_2WO_4 and WO_3 obviously and no additional peaks are detected. The results indicate that the existence of RGO does not affect the growth of new crystal orientations of Ag_2WO_4/WO_3, and the AWR photocatalysts were successfully fabricated by the facile hydrothermal approach.

SEM images of RGO (a), pure WO_3 (b), Ag_2WO_4 (c), Ag_2WO_4/WO_3 (d), AWR-2 (e) and EDS spectrum of AWR-2 (f) are shown in Figure 2. As can be seen from the Figure 2a, RGO nanosheets are curled and corrugated, which is consistent with the previous report [7], while WO_3 hollow spheres sample shows the uniform particle size (Figure 2b). The pristine Ag_2WO_4 exhibits regular particle morphology with an average size of 150 nm in diameter and 20 μm in length (Figure 2c), and the surface is relatively smooth without any secondary nanostructures, indicating a high uniformity of the rod-like morphology. From Figure 2d, it could be found from that Ag_2WO_4 nanoparticles are successfully decorated on the WO_3 spheres surface and exhibits that the unique shape and the hollow sphere was not destroyed. As can be seen from Figure 2e, it seems that large amounts of Ag_2WO_4/WO_3 particles are distributed on the surface of RGO sheets, indicating a good loading between Ag_2WO_4/WO_3 and RGO. SEM images illustrate the transparent properties of the RGO substrate, where the RGO retains its two-dimensional thin sheet structure with wrinkled regions after loading of the Ag_2WO_4/WO_3. This structure might provide enough contact surface area between the RGO sheets and Ag_2WO_4/WO_3 particles and presumably facilitate charge-carrier transport. EDS spectrum (Figure 2f) shows that all the points in the selected area display the existence of Ag, W, O and C elements. The 2D-projected elemental mapping

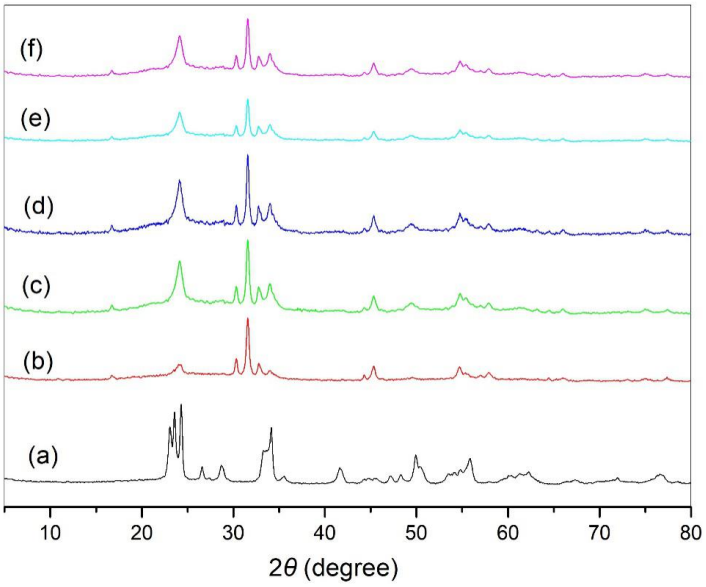

FIGURE 1
XRD patterns of pure WO_3 (a), Ag_2WO_4 (b), Ag_2WO_4/WO_3 (c), AWR-1 (d), AWR-2 (e) and AWR-1(f) photocatalysts

demonstrates the distribution of these elements throughout the AWR-2 sample.

Raman spectra of Raman spectra of RGO (a), pure WO_3 (b), Ag_2WO_4 (c), Ag_2WO_4/WO_3 (d) and AWR-2 (e) photocatalyst are shown in Figure 3. As shown in Figure 3 (a and e), two observably peaks at about 1330~1340 and 1580~1593 cm^{-1} are defined as D band and G bands of RGO in the spectra of pure RGO and photocatalyst, corresponding to the E_{2g} phonon of sp^{2-} bonded carbon atoms in a two-dimensional hexagonal lattice, as well as the defects and disorder carbon in the graphite layers, respectively [7]. As for bare WO_3, the bands centered at 808 cm^{-1} and 715 cm^{-1} are attributed to W-O stretching (Figure 3 b, d and e). The sharp peak located at about 881 cm^{-1} are observed in spectrum of pure Ag_2WO_4 and AWR-2 photocatalyst (Figure 3 c and e), which is attributed to the WO_4^{2-} symmetric stretching vibration. In addition, O-W-O stretching is revealed at the band centered at about 273cm^{-1}. For the AWR-2, all the Raman bands for RGO, Ag_2WO_4 and WO_3 can be observed confirming the presence of RGO, Ag_2WO_4 and WO_3 in the composites, which further suggests the decoration of Ag_2WO_4 and WO_3 on the RGO surface. The obtained Raman spectrum result of AWR-2 indicates that AWR-2 photocatalyst was successfully obtained.

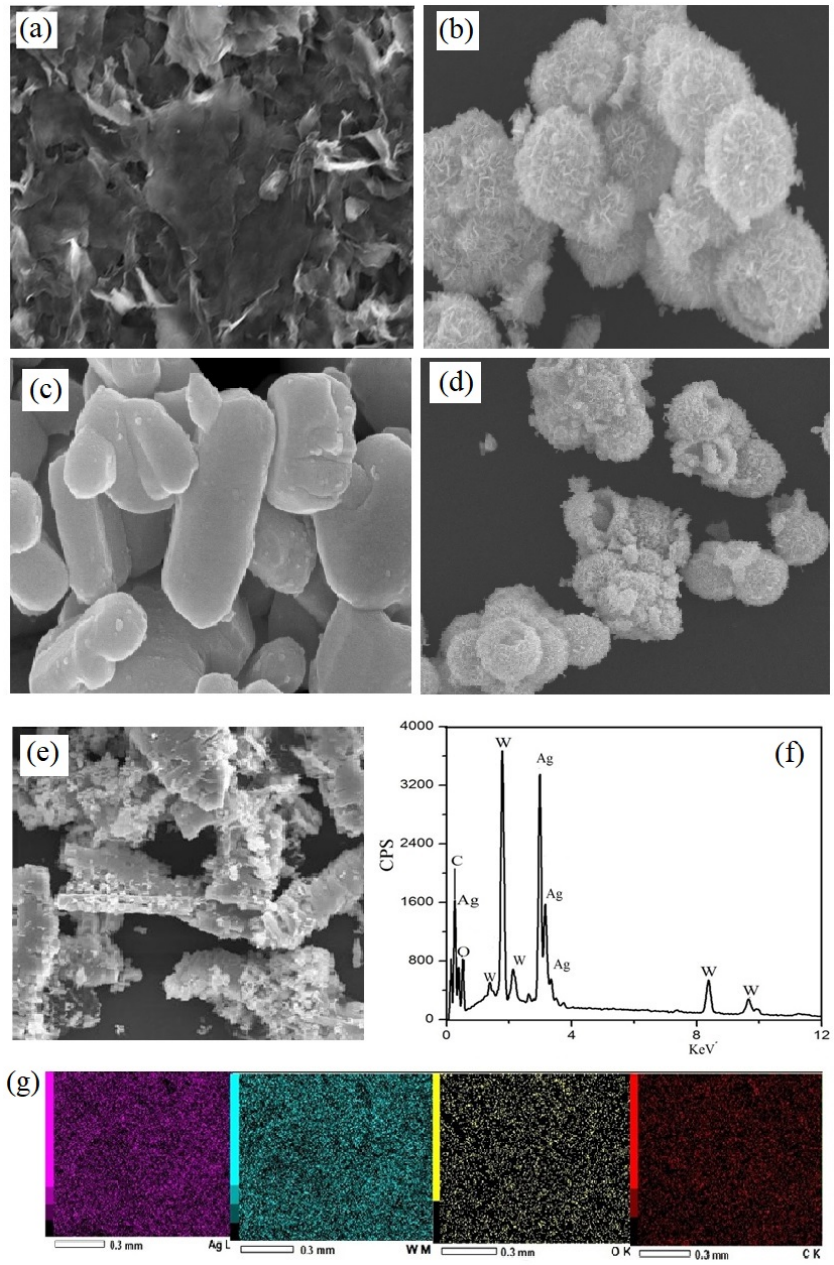

FIGURE 2
SEM images of RGO (a), pure WO_3 (b), Ag_2WO_4 (c), Ag_2WO_4/WO_3 (d), AWR-2 (e) and EDS spectrum of AWR-2 (f); The corresponding elemental mappings (g) of Ag, W, O and C elements

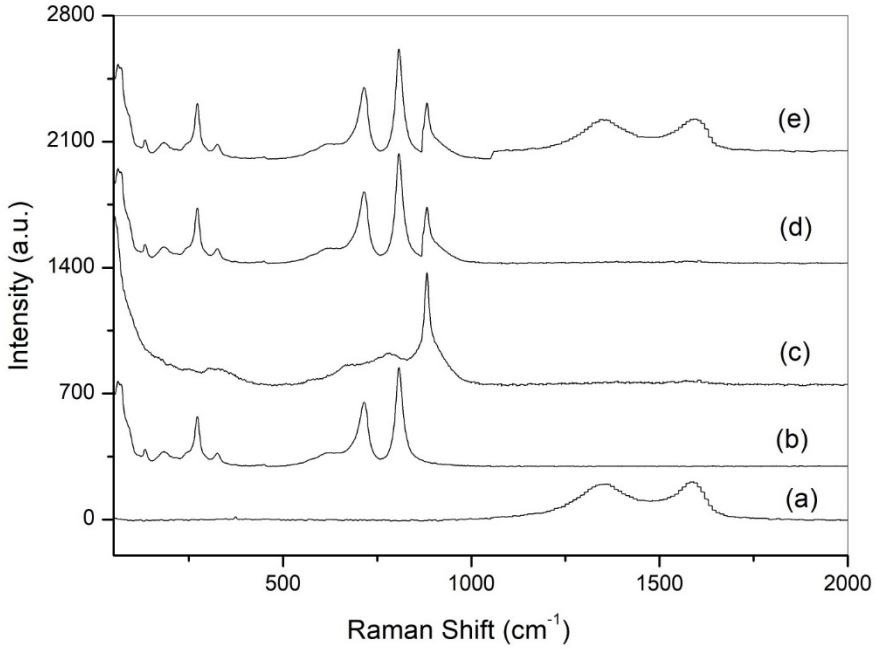

FIGURE 3
Raman spectra of RGO (a), pure WO_3 (b), Ag_2WO_4 (c), Ag_2WO_4/WO_3 (d) and AWR-2 (e)

More detailed information regarding the chemical and bonding environment of the composites are ascertained by XPS. Fig.4 shows the XPS spectra of AWR-2. From Figure 4a, the survey XPS spectrum shows the coexistence of elements, Ag, W, O and C; and no other hetero-elements were detected. As can be seen from Ag3d XPS, the peaks located at 373.66 and 368.23 eV are assigned to Ag $3d_{3/2}$ and Ag $3d_{5/2}$, respectively, further confirming the existence of Ag^+. From C 1s and O 1s XPS core level spectra, the peaks at the banding energy of 289.68 and 531.73 eV are attributed to oxygen and carbon, respectively. In the high-resolution spectrum of W 4f, the binding energy of W4f is 35.23eV, which agrees with W^{6+} ion of the sample. These results confirmed that the catalysts AWR-2 could be prepared by a facile hydrothermal method.

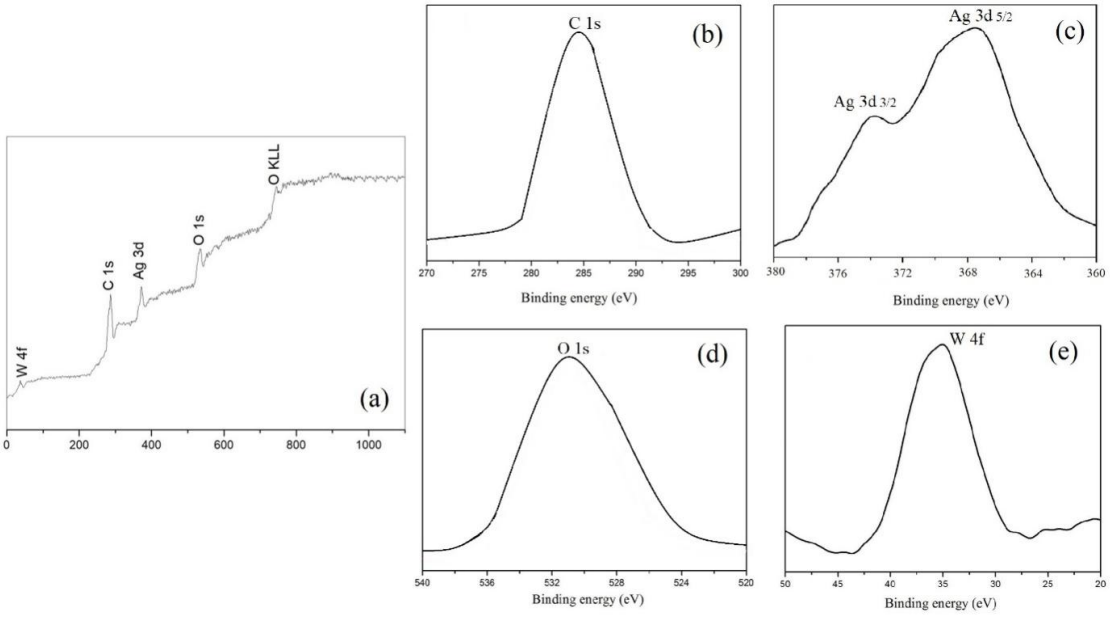

FIGURE 4
XPS spectra of AWR-2 (a), C 1s (b), Ag3d (c), O1s (d) and W4f (e)

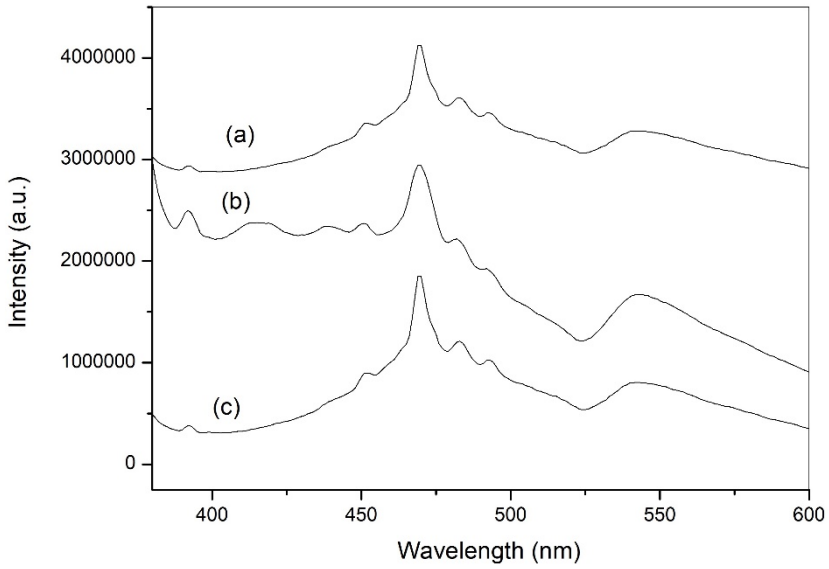

FIGURE 5
PL emission spectra of WO_3 (a), Ag_2WO_4 (b) and AWR-2 (c) photocatalysts

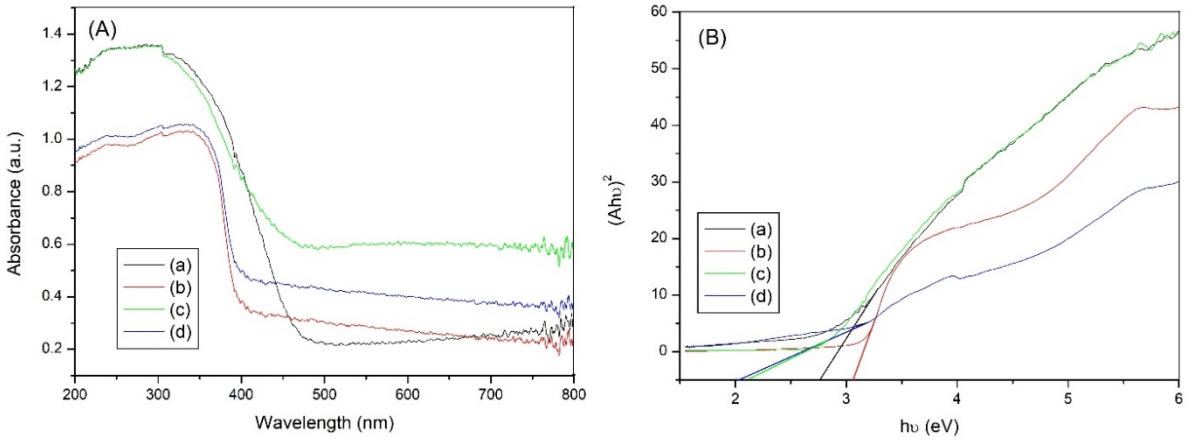

FIGURE 6
(A) UV-vis diffuse reflectance spectra of WO_3 (a), Ag_2WO_4 (b), Ag_2WO_4/WO_3 (c) and AWR-2 (d) photocatalysts; (B) Plots of $(h\nu)^2$ vs. (B) photonenergy (hν) of WO_3 (a), Ag_2WO_4 (b), Ag_2WO_4/WO_3 (c) and AWR-2 (d)

PL spectra are useful to disclose the migration, transfer, and recombination processes of the photogenerated electron-hole pairs in semiconductors. In general, the lower PL intensity indicates a decrease in the recombination rate of photogenerated charge carriers. The better separation of photogenerated electrons and holes in the AWR photocatalyst is confirmed by PL emission spectra of single Ag_2WO_4, WO_3 and AWR-2 photocatalyst; and PL emission spectra of bare WO_3 (a), Ag_2WO_4 (b) and AWR-2 (c) photocatalysts recorded with an excitation wavelength at 363 nm are shown in Figure 5. As can been from Figure 5, the strong emission peaks of the bare WO_3 and Ag_2WO_4 are located at about 469 and 470 nm, which could be attributed to a band-to-band emission. Compared with single WO_3 and Ag_2WO_4, the emission peak intensity of the AWR-2 photocatalysts decrease moderately, indicating that the recombination of photogenerated charge carriers is suppressed. The result of PL verifies that the AWR photocatalysts could effectively separate photogenerated electron-hole pairs.

The optical absorption properties of the as-prepared samples are examined by UV-vis diffuse reflectance spectra since the optical absorption behavior of a photocatalyst was essential for its photocatalytic activity, and the results are shown in Figure 6. As shown in Figure 6A, the AWR photocatalysts exhibit broad absorption in the whole visible region and its absorption intensity is strengthened. This is mainly because introduction of RGO leads to an obvious enhancement of background absorption in the range of 500-800 nm. In addition, the optical band

gap and absorption coefficient of semiconductor can be calculated by the following equation [11]: $(\alpha hv)^n = A(hv - E_g)$, where α, h, v, E_g and A are the absorption coefficient, Planck's constant, light frequency, band gap and a constant, respectively. n is a constant associated with different kinds of electronic transitions (n=0.5 for a direct allowed and n=2 for an indirect allowed). From the Figure 6B, the band gaps of WO_3, Ag_2WO_4, Ag_2WO_4/WO_3 and AWR-2 samples are about 2.75, 3.07, 2.06 and 2.04 eV, respectively. This observation indicates that the introduction of RGO narrows the band gap of Ag_2WO_4/WO_3. Therefore, the formation rate of electron-hole pairs on the photocatalyst surface/interfaces also increases substantially, resulting in the better catalytic performance.

To further obtain the pore size distributions and specific surface area of the prepared samples, N_2 adsorption-desorption measurements were performed. N_2 adsorption-desorption isotherms and pore-size distribution curves of WO_3 (a), Ag_2WO_4 (b), Ag_2WO_4/WO_3 (c) and AWR-2 (d) are shown in Figure 7. From Figure 7A, the measured BET specific surface areas of WO_3, Ag_2WO_4, Ag_2WO_4/WO_3 and AWR-2 are 13.23, 1.36, 15.21 and 18.99 $m^2\ g^{-1}$, respectively. Meanwhile, the corresponding pore volume distributions of both samples were calculated by the BJH method from the adsorption branch of the isotherms. As shown in Figure 7B, average pore sizes of WO_3, Ag_2WO_4, Ag_2WO_4/WO_3 and AWR-2 are 22.3, 17.22, 20.23 and 15.28 nm, respectively. Therefore, the increase in surface area of composite material can provide more possibility for the efficient adsorption and mass transfer for the degradable dye molecules and hydroxyl radicals the photochemical reaction. This phenomenon favors for the enhancement in photocatalytic activity.

Photocatalytic activity. The photocatalytic oxidation activity of as-synthesized photocatalysts has been evaluated using MB as the model pollutant; and the results are shown in Figure 8a. For comparison, the blank test was also conducted under the

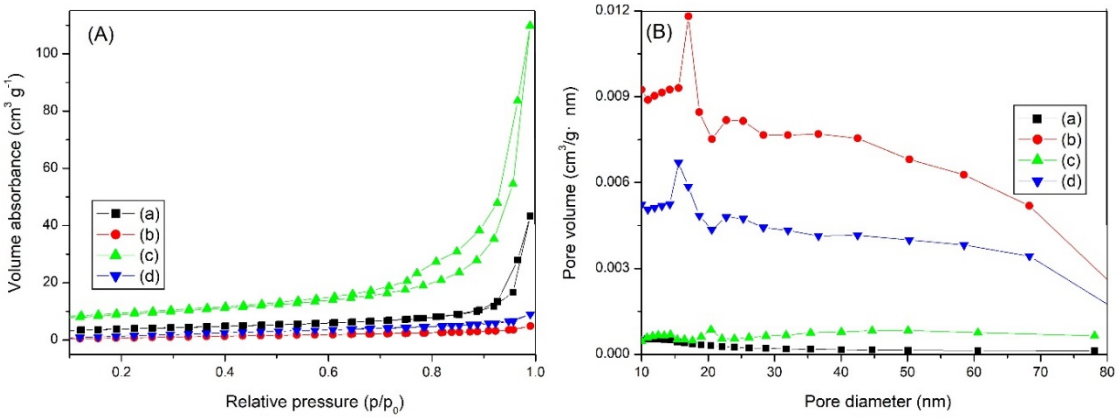

FIGURE 7
(A) N_2 adsorption-desorption isotherms and (B) pore-size distribution curves of WO_3 (a), Ag_2WO_4 (b), Ag_2WO_4/WO_3 (c) and AWR-2 (d) photocatalysts

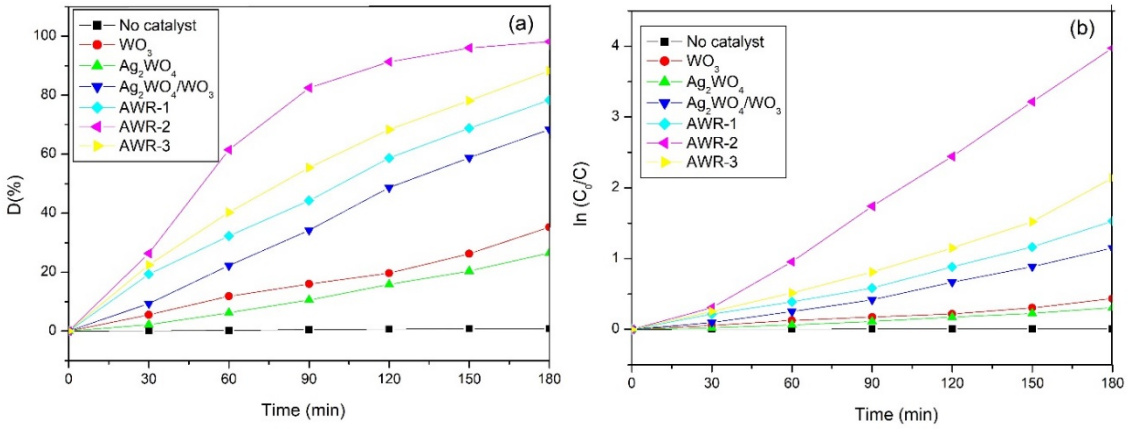

FIGURE 8
Comparison of the photocatalytic activities of samples for degradation of the MB solution

same reaction conditions. It could be seen that negligible photodegradation of MB observed when no catalyst is added. About 35%, 26% and 68% of the MB were respectively removed by WO_3, Ag_2WO_4 and Ag_2WO_4/WO_3 after 180 min of visible light irradiation. Absolutely, the photocatalytic activities of all AWR photocatalysts are higher than those of the WO_3, Ag_2WO_4 and Ag_2WO_4/WO_3 and about 98.15% MB was removed by AWR-2 in 180 min. It may be because of the formation of recombination centers of photoinduced carriers in the bulk of the catalyst [13]. The linear relationship between $\ln C_0/C$ and t of the as-prepared photocatalysts is shown in Figure 8b, which confirming that the photodegradation reaction of MB dye is fitted pseudo-first-order. According to Eq.(2) and Figure 8b, the pseudo-first-order rate constant of photodegradation are 0.0000562 min^{-1}, 0.00225 min^{-1}, 0.00172 min^{-1}, 0.00649 min^{-1}, 0.00832 min^{-1}, 0.0229 min^{-1} and 0.0115min^{-1} for no catalyst, WO_3, Ag_2WO_4, Ag_2WO_4/WO_3, AWR-1, AWR-2 and AWR-3, respectively. Clearly, the AWR-2 reveals the highest value with k. The stability of a photocatalyst is important for its assessment and application. Recycling experiments were performed to check the stability of photocatalyst. Comparison of photocatalytic performance within 5 cycles for AWR-2 photocatalyst under the same experimental condition is shown in Figure 9. As can be seen from Figure 10, the degradation of photocatalyst has no observable change even after 5 recycles. The results indicated that the prepared photocatalyst has an excellent reuse performance.

The possible mechanism. According to the above results, a proposed mechanism is shown in Figure 10. Under visible light irradiation, plasmon-excited WO_3 and Ag_2WO_4 can produce photogenerated electrons and holes. The photogenerated holes (h^+) and electrons (e^-) transfer to the surface of Ag_2WO_4/WO_3 and then drive photocatalytic oxidation reactions. O_2^-• radicals are produced by the reduction of O_2 molecules adsorbed on the catalyst surface by the photogenerated electrons. In addition, the reaction of H_2O and active holes generate ·OH, and both O_2^-• and ·OH radicals can degrade organic dye (MB) effectively. Due to the introduction of RGO and the close interfacial contact, the photogenerated electrons on the conduction band (CB) of Ag_2WO_4/WO_3 could be effectively transferred to the RGO sheets. These synergistic interaction between the SPR of WO_3 and the field around Ag_2WO_4 can force the photogenerated electrons in Ag_2WO_4/WO_3 particles under visible-light irradiation to produce photogenerated electron-hole pair separation and photogenerated charge transfer. Therefore, the formation rate of electron-hole pairs on the sample increases substantially, exhibiting excellent photocatalytic performance. Moreover, high surface area RGO sheets offer more active adsorption sites and photocatalytic reaction sites, which also favor improved photocatalytic activity. According to these results, one important conclusion can be drawn, that is, when discussing the effect of introduction graphene or RGO on the photocatalytic activities of semiconductor particles, the results should be analyzed based on specific reactions.

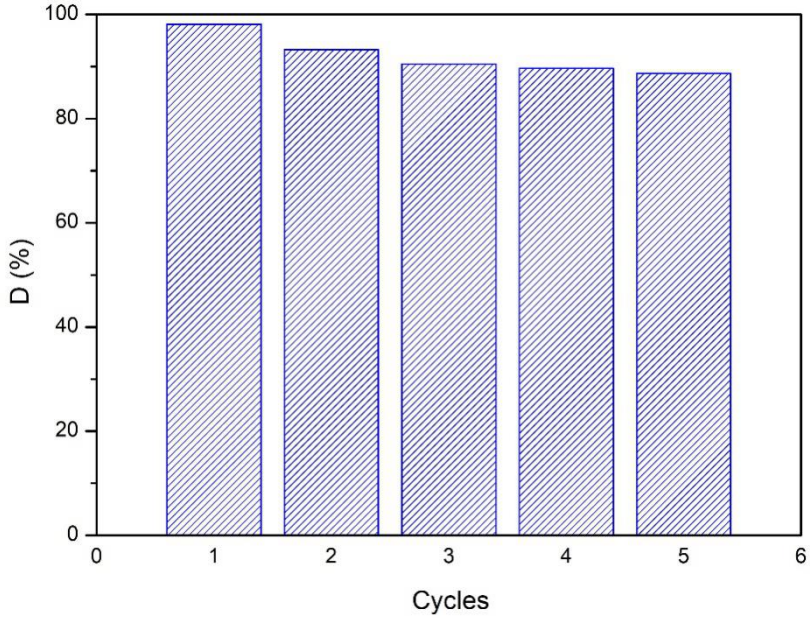

FIGURE 9
Cycling test of AWR-2 for the degradation of MB under visible light irradiation

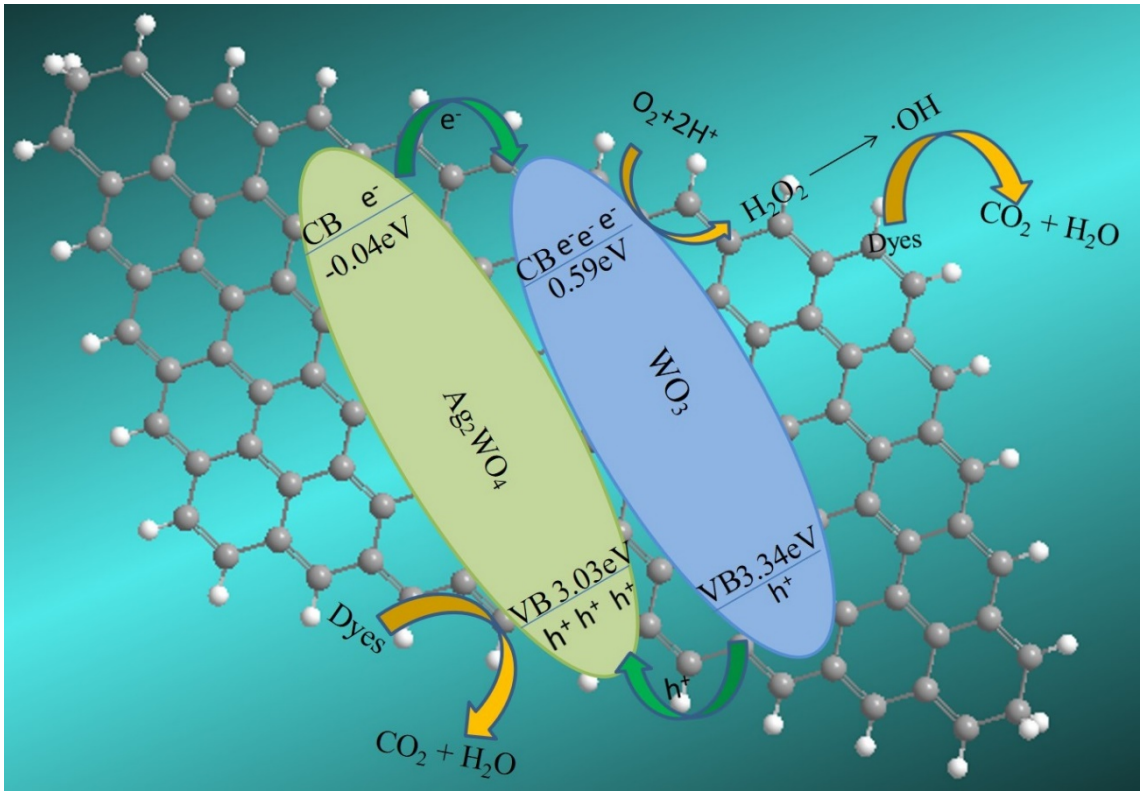

FIGURE 10
Proposed mechanism of enhanced photocatalytic activity for the AWR photocatalyst

CONCLUSION

In summary, Ag_2WO_4/WO_3/RGO photocatalysts (AWR) were synthesized with a facile hydrothermal method. The AWR photocatalyst was characterized by using XRD, SEM, Raman, Brunauer-Emmett-Teller, photoluminescence, XPS and UV-Vis DRS; and shows excellent performance in the degradation of MB under visible light irradiation. It is found that suitable content of Ag_2WO_4/WO_3 in AWR photocatalyst is crucial optimize the photocatalytic performance. Among the series of AWR photocatalysts, AWR-2 shows the highest photocatalytic activity, and degradation conversion of MB is high up to 98.15% under visible light irradiation. The enhanced photocatalytic activity of the AWR photocatalyst can be attributed to the synergy effect between Ag_2WO_4/WO_3 and RGO, which facilitates interfacial charge transfer and inhibits electron-hole recombination. This AWR photocatalyst material may have potential applications in pollutant removal as highly efficient photocatalyst.

ACKNOWLEDGEMENT

This work was financially supported by Jiangsu Planned Projects for Postdoctoral Research Funds (2020Z098), National Natural Science Foundation of China (21901119, 41471191), China Postdoctoral Science Foundation Funded Project (2019M661850), Projects of National Key Research and Development of China (2017YFC0505803), Qing Lan Project of Jiangsu Province (Qinglan 2016-15), Priority Academic Program Development of Jiangsu Higher Education Institutions (PAPD), Students Practice Innovation and Training Program of Nanjing Forestry University (2019NFUSPITP0761, 2020NFUSPITP0804, 2020NFUSPITP0807, 2020NFUSPITP0818, 2020NFUSPITP0827) and the Analysis and Test Center of Nanjing Forestry University.

REFERENCES

[1] Wu, G., Xing, W. (2019) Facile preparation of semiconductor silver phosphate loaded on multi-walled carbon nanotube surface and its enhanced catalytic performance, Journal of Inorganic and Organometallic Polymers and Materials. 29, 617-627.

[2] Xing, W., Yin, S., Tu, W., Liu, G., Wu, S., Wang, H., Kraft, M., Wu, G., Xu, R. (2020) Rational synthesis of amorphous iron-nickel phosphonates for highly efficient photocatalytic water oxidation with almost 100 % yield. Angewandte Chemie International Edition. 59, 1171-1175.

[3] Meng, Q., Lv, C., Sun, J., Hong, W., Xing, W., Qiang, L., Chen, G., Jin, X. (2019) High-efficiency Fe-Mediated Bi_2MoO_6 nitrogen-fixing photocatalyst: Reduced surface work function and ameliorated surface reaction. Applied Catalysis B: Environmental. 256, 1-41. Article ID: 117781.
[4] Lv, J., Dai, K., Zhang, J., Lu, L., Liang, C., Geng, L., Wang, Z., Yuan, G., Zhu, G. (2017) In situ controllable synthesis of novel surface plasmon resonance-enhanced $Ag_2WO_4/Ag/Bi_2MoO_6$ composite for enhanced and stable visible light photocatalyst. Applied Surface Science. 391, 507-515.
[5] Vignesh, K., Kang, M. (2015) Facile synthesis, characterization and recyclable photocatalytic activity of Ag_2WO_4@g-C_3N_4. Materials Science & Engineering B. 199(5), 30-36.
[6] Ren, H.T., Jia, S.Y., Wu, S.H., Zhang, T.H., Han, X. (2015) Phase transformation synthesis of novel Ag_2O/Ag_2CO_3/g-C_3N_4 composite with enhanced photocatalytic activity. Materials Letters. 142, 15-18.
[7] Wu, G., Xing, W. (2019) Facile and fabrication of semiconductor silver tungstate loaded on the graphene oxide surface and its effective enhanced catalytic performance. Fresen. Environ. Bull. 28(3), 2012-2021.
[8] Guo, S., Dong, S. (2011) Graphene nanosheet: synthesis, molecular engineering, thin film, hybrids, and energy and analytical applications. Chemical Society Reviews. 40(5), 2644-2672.
[9] Low, J., Cao, S., Yu, J., Wageh, S. (2014) Two-dimensional layered composite photocatalysts, Chemical Communications. 50(74), 10768-10777.
[10] Bo, C., Jing, L., Qian, X. (2014) Reduced graphene oxide grafted Ag_3PO_4 composites with efficient photocatalytic activity under visible-light irradiation, Industrial & Engineering Chemistry Research. 53(21), 8744–8752.
[11] Wu, G., Xing, W. (2019) Fabrication of ternary visible-light-driven semiconductor photocatalyst and its effective photocatalytic performance. Materials Technology. 34, 292–300.
[12] Rong, X., Qiu, F., Zhang, C., Fu, L., Wang, Y., Yang, D. (2015) Adsorption–photodegradation synergetic removal of methylene blue from aqueous solution by NiO/graphene oxide nanocomposite. Powder Technology. 275, 322-328.
[13] Qiu, F., Zhu, X., Guo, Q., Dai, Y., Xu, J., Zhang, T. (2017) Fabrication of a novel hierarchical flower-like hollow structure Ag_2WO_4/WO_3 photocatalyst and its enhanced visible-light photocatalytic activity, Powder Technology. 317, 287-292.

Received: **29.08.2020**
Accepted: **06.11.2020**

CORRESPONDING AUTHOR

Weinan Xing
College of Biology and the Environment,
Co-Innovation Center for the Sustainable Forestry in Southern China,
Nanjing Forestry University,
Nanjing 210037 – China

e-mail: xingwn@njfu.edu.cn